

High-Order Flux Reconstruction on Stretched and Warped Meshes

Will Trojak,* Rob Watson,† and Paul G. Tucker‡

University of Cambridge, Cambridge, England CB2 1PZ, United Kingdom

DOI: 10.2514/1.J056341

High-order computational fluid dynamics is gathering a broadening interest as a future industrial tool, with one such approach being flux reconstruction (FR). However, due to the need to mesh complex geometries if FR is to displace current lower-order methods, FR will likely have to be applied to stretched and warped meshes. Therefore, it is proposed that the analytical and numerical behaviors of FR on deformed meshes for both the one-dimensional linear advection and the two-dimensional Euler equations are investigated. The analytical foundation of this work is based on a modified von Neumann analysis for linearly deformed grids, which is presented. The temporal stability limits for linear advection on such grids are also explored analytically and numerically, with Courant–Friedrichs–Lewy (CFL) limits set out for several Runge–Kutta schemes, with the primary trend being that contracting mesh regions give rise to higher CFL limits, whereas expansion leads to lower CFL limits. Lastly, the benchmarks of FR are compared to finite difference and finite volumes schemes, as are common in industry, with the comparison showing the increased wave propagating ability on warped and stretched meshes, and hence FR's increased resilience to mesh deformation.

Nomenclature

a	=	convective velocity
C_0	=	center cell flux reconstruction matrix
C_{-1}	=	upwind cell flux reconstruction matrix
$c(k)$	=	phase velocity at wave number k
D	=	first derivative matrix
f	=	flux variable in physical domain
$\hat{G}(\hat{k})$	=	computational filter kernel
h_l, h_r	=	left and right correction functions
J_n	=	n th cell Jacobian
k	=	wave number
k_{nq}	=	solution point Nyquist wave number; $(p + 1)/\delta_j$
\hat{k}	=	k_{nq} normalized wave number; $[0, \pi]$
l_n	=	n th Lagrange basis function
p	=	solution polynomial order
Q	=	spatial scheme matrix
R	=	update matrix
u	=	primitive in physical domain
\tilde{u}	=	Fourier reconstructed field
γ	=	grid geometric expansion factor
δ_j	=	mesh spacing; $x_j - x_{j-1}$
ϵ	=	points per wave number error level
ξ	=	transformed spatial variable
$\rho(A)$	=	spectral radius of A
τ	=	time step
Ω	=	solution domain
Ω_n	=	n th solution subdomain
Ω_s	=	standardized subdomain

Subscripts

l	=	variable at left of cell
r	=	variable at right of cell

Superscripts

c	=	common value at interface
T	=	vector or matrix transpose
δ	=	discontinuous value
\wedge	=	transformed variable
$-$	=	locally fitted polynomial of variable

I. Introduction

THE potential of large-eddy simulations (LESs) has been understood for some time; however, most current industrial LES and Reynolds-averaged Navier–Stokes (RANS) implementations make use of second-order spatial schemes. This kind of lower spatial order for LESs can be prohibitively expensive in some flow regimes, with cost scaling (from Piomelli [1]) with $\sim Re^{2.4}$ for the innermost section of the boundary layer. Figure 1 aims to show that, for a gas turbine engine, a conventional LES has a much larger overhead than a hybrid RANS–LES, with the full LES only really being currently feasible in the lower-pressure turbine stages. The Reynolds number, Re , is also plotted, showing that large variations in flow regimes occur (see Tucker et al. [2]). This shows that, with current methods, the LES is only routinely used for the low-pressure turbines. Data presented later can give an estimate of the three-dimensional mesh requirement for fourth-order flux reconstruction. From the metrics to be shown later, using flux reconstruction (FR) could make the conventional LES far cheaper. The high cost of wall-resolved LESs originates from all but 10–20% of the vortical motions being directly simulated in both space and time (Tucker [3]). The unresolved fraction of the vortical motion must therefore be accounted for using a subgrid-scale model. As LESs will make use of finite discretizations on the underlying equation [be that through a finite volume (FV), a discontinuous Galerkin, or another method], the solution will incur truncation and aliasing errors. Therefore, for the subgrid-scale model to correctly influence the flow, the subgrid-scale error must be minimized. This area was explored by Chow and Moin [4] and Ghosal [5], who found that, for a second-order central finite difference (FD) LES, the filter width was needed to be four times the grid spacing. They also found that, for an eighth-order central FD LES, a filter width of twice the grid spacing was required. This effect occurred because, for second-order schemes, the numerical error and the subgrid-scale forcing would have same-order scaling with respect to the grid spacing, whereas a move to a higher order meant the differencing error order increased, and so the filter scale could decrease. Regardless, higher orders allow for coarser meshes to capture the same flow regime, and they can reduce the high computational barrier to the use of the LES. Hence, high-order methods have become of increasing interest for the industry. For

Presented as Paper 2017-0521 at the 55th AIAA Aerospace Sciences Meeting, AIAA SciTech Forum, Grapevine, TX, 9–13 January 2017; received 19 May 2017; revision received 29 March 2018; accepted for publication 31 July 2018; published online 16 November 2018. Copyright © 2018 by Will Trojak, Rob Watson, and Paul G. Tucker. Published by the American Institute of Aeronautics and Astronautics, Inc., with permission. All requests for copying and permission to reprint should be submitted to CCC at www.copyright.com; employ the ISSN 0001-1452 (print) or 1533-385X (online) to initiate your request. See also AIAA Rights and Permissions www.aiaa.org/randp.

*Ph.D. Candidate, Department of Engineering, Student Member AIAA.

†Research Fellow, Department of Engineering, Member AIAA.

‡Professor, Department of Engineering, Associate Fellow AIAA.

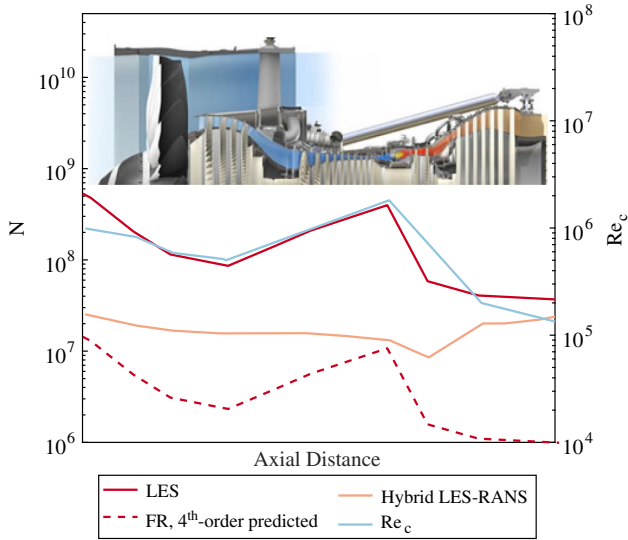


Fig. 1 LES and hybrid RANS-LES mesh degrees-of-freedom requirement against axial distance through a gas turbine engine.

example, studying the abstracts of the AIAA SciTech Conferences on Aerospace Sciences shows an increase from 62 to 99 papers that used or studied high-order methods between 2014 and 2015.

Huynh [6] introduced a high-order scheme that he termed flux reconstruction, and this has since evolved into a wider family of schemes explored by Vincent et al. [7] using energy stability arguments to define a wide family of correction functions. Extensions have been made to handle advection–diffusion [8,9], simplex and hypercube elements [10–12], and various optimizations of the collocation points and correction functions [13–15]. The quantitative evaluation performed analytically and numerically had largely been confined to canonical meshes; and the scenarios explored, although of great importance, were often of less direct relevance to computational fluid dynamics (CFD) practitioners. This was due to their contrived nature leading to well-presented problems, which were useful as benchmarks but did not always show the full picture. In essence, it was common for the actual problems encountered by engineers to be highly complex, making meshes with low levels of skew or low-level interelement expansion very difficult to produce. Furthermore, FR was rooted in finite element methods, and consequently was an unstructured approach that fundamentally enabled far more irregularities within the mesh as compared to structured approaches. This highlighted the importance of accurate characterization of the scheme on irregular meshes.

Previous investigations into the analytical behavior of numerical methods on irregular grids have been confined to schemes such as the finite difference, in which the mesh transformation can be more easily applied. For example Chung and Tucker [16], in whose work the effect of hyperbolically transformed grids was investigated for FD and compact FD schemes, clearly demonstrated the added dissipation that transformation could cause. More recently, You et al. [17] demonstrated a more thorough approach, detailing the exact higher-order terms that led to inaccuracy on hyperbolically skewed grids. Within the field of FR, some numerical results have been presented pertaining to the accuracy of FR applied to curvilinear grids (Mengaldo et al. [18]), and they showed some interesting parallels between the FR and discontinuous Galerkin methods. This did, however, limit the quantification to numerical experiments that, although very powerful, did not allow the bedrock of the scheme to be exposed. Further investigation into the effect of curvilinear grids on the Jacobian was presented by Kopriva [19]. Lastly, FR coupled to r -type mesh adaptation was performed by Sheshadri et al. [20] for the purposes of shock capture using a “divide or conquer” method that showed reasonable performance. These works have laid a fine basis for the development of study into the effect of mesh transformation on finite element schemes and, in this case, for FR.

The aims of this paper are broken down into several sections. An analytical framework is constructed using the established von Neumann analysis; however, the generality of the grid will be maintained such that nonuniform grids may be investigated. The subsequent analytical investigations are concerned with the dispersion and dissipation of various orders of FR for nonuniform one-dimensional (1-D) grids, as well as with moving on to couple the spatial scheme to a temporal scheme to establish theoretical Courant–Friedrichs–Lewy (CFL) limits for various grids. A numerical methodology is proposed such that the analytical results may be validated, also enabling evaluation of the fully discretized spatial–temporal scheme. Lastly, the numerical investigation is taken further, into two dimensions (2-D), using the Euler equations to understand the behavior of more relevant flows on meshes that have been artificially degraded. This test case can also enable a comparison to be made to a more prevalent industrial FV scheme.

II. Flux Reconstruction

Flux reconstruction [6,21] applied to the linear advection equation will form the basis of the initial investigation to be carried out and, for the readers’ convenience, an overview of the scheme is presented here. However, for a more detailed understanding, the reader should consult the works of Castonguay [21] or Huynh [6]. This 1-D scheme can be readily converted to two dimensions (carried out later) and three dimensions for quadrilaterals and hexahedrals, respectively. First, let us consider the one-dimensional advection equation:

$$\frac{\partial u}{\partial t} + \frac{\partial f}{\partial x} = 0 \quad (1)$$

The FR method is related to the discontinuous Galerkin method [22] and uses the same subdivision of the domain into discontinuous subdomains:

$$\Omega = \bigcup_{n=1}^N \Omega_n \quad (2)$$

In the standardized subdomain $\Omega_s \in \mathbb{R}^d$, computational spatial variables are defined. When $d = 1$, $\Omega_s = [-1, 1]$, using ξ to denote the value taken. This computational space is discretized with $(p + 1)^d$ solution points, and $2d(p + 1)^{d-1}$ flux points are placed at the edges of the subdomain. (Figure 2a shows a 1-D example.) To transform from $\Omega_n \rightarrow \Omega_s$, the Jacobian J_n is defined such that

$$\hat{u}^\delta = \hat{u}^\delta(\xi; t) = J_n u^\delta(x; t) \quad (3)$$

and the solution point mapping in the physical domain used throughout this investigation results in the Jacobian representing a linear mapping. With the domain setup, we now proceed with defining the steps to construct a continuous solution from discontinuous segments. The first stage is to define a local solution polynomial in Ω_s using Lagrange interpolation:

$$l_k(\xi) = \prod_{i=1, i \neq k}^{p+1} \frac{\xi - \xi_i}{\xi_k - \xi_i} \quad (4)$$

$$\hat{u}^\delta(\xi; t) = \sum_{i=1}^{p+1} \hat{u}_i^\delta l_i(\xi) \quad (5)$$

Repeating the interpolation for the discontinuous flux in Ω_s ,

$$\hat{f}^\delta = \hat{f}^\delta(\xi; t) = \sum_{i=1}^{p+1} \hat{f}_i^\delta l_i(\xi) \quad (6)$$

Now, using the Jacobian and the solution polynomials, the primitive and flux values can be approximated in the physical domain Ω_n :

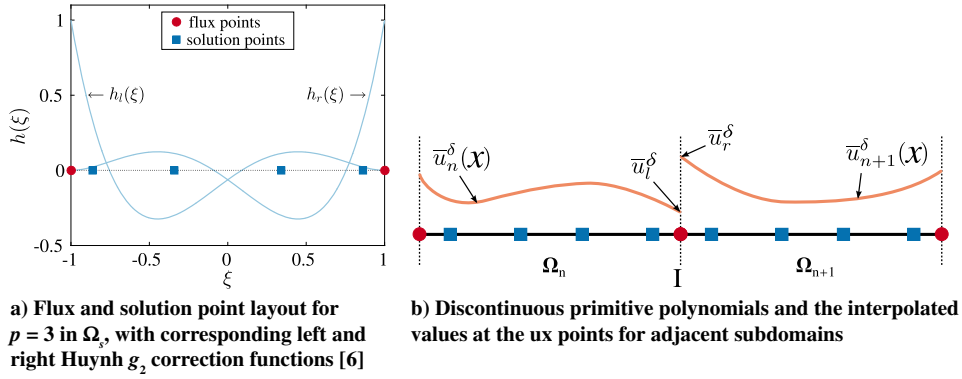


Fig. 2 Point layout in Ω_s for $p = 3$ and cell interface topology.

$$\bar{u}^\delta(x; t) = \frac{\hat{u}^\delta(\xi; t)}{J_n} \quad (7)$$

This distinction is made due to the potentially approximate nature of J_n . However, for the case of linear transformations, as will be considered here, J_n fully captures the spatial transformation, and thus \bar{u}^δ will be a polynomial of order p . With a polynomial formed in the reference domain, the value of the primitive at the flux points (see Fig. 2a) can be defined as $\hat{u}_l^\delta = \hat{u}^\delta(-1)$ and $\hat{u}_r^\delta = \hat{u}^\delta(1)$; this can be repeated for the flux values. Once the primitive values at the interface I have been interpolated, a common interface flux can be calculated \hat{f}_I^c in the physical domain. For a general case, this is done using a Riemann solver on the primitives at the interface, such as those of Roe [23]; flux-vector splitting [24]; or the Harten–Lax–van Leer [25]. To get a spatially continuous solution over Ω , the common interface flux must be incorporated into the solution. For FR, this is done by using a correction function to propagate the corrected flux gradient into the Ω_n . Figure 2a shows the correction function proposed by Huynh [6] and, in general, the left and right correction functions are defined as $h_l(\xi)$ and $h_r(\xi)$. The procedure to apply the correction to transformed discontinuous flux in Ω_s is as follows:

$$\frac{\partial \hat{f}(\xi_i)}{\partial \xi} = \sum_{j=1}^{p+1} \hat{f}_j \frac{d\mathbf{l}_j(\xi_i)}{d\xi} + (\hat{f}_l^c - \hat{f}_l^\delta) \frac{dh_l(\xi_i)}{d\xi} + (\hat{f}_r^c - \hat{f}_r^\delta) \frac{dh_r(\xi_i)}{d\xi} \quad (8)$$

This then allows the transformed continuous equation to be written as follows:

$$\frac{\partial \hat{u}(\xi_i)}{\partial t} = - \frac{\partial \hat{f}(\xi_i)}{\partial \xi} \quad (9)$$

and hence the solution can be advanced in time via some method of temporal integration.

III. Von Neumann Analysis

The main analysis to be carried out is a von Neumann analysis that follows the work of Lele [26], Hesthaven and Warburton [27], Huynh [6], Vincent et al. [7], and Asthana and Jameson [14]. The analysis shown here differs from that of previous work, in that it does not assume that the grid is uniform and instead retains generality: the advantage being that the effect of grid stretching can be investigated. For the analysis, consider the computational domain as before, $\Omega \in \mathbb{R}^1$ with $N - 1$ subdomains Ω_n , with flux points of Ω_n located at $\mathbf{x}_j \forall j \in \mathbb{N}, j \leq N$. The 1-D linear advection equation can be written as in Eq. (10):

$$\frac{\partial u}{\partial t} + a \frac{\partial u}{\partial x} = 0 \quad (10)$$

Projecting Eq. (10) onto the space Ω and combining Eqs. (8) and (9) result in the following:

$$\frac{\partial \bar{u}_j}{\partial t} = -J_j^{-1} \left(\mathbf{D} \mathbf{f}_j + (f_l^c - f_j(x_j)) \mathbf{h}_l + (f_r^c - f_j(x_{j+1})) \mathbf{h}_r \right) \quad (11)$$

The notation used is compatible with that set out initially in [7], taking D_{mn} as the contribution from the first derivative on the m th Lagrange basis function to the n th solution point. Note that \mathbf{h}_l and \mathbf{h}_r are taken as $dh_l(\xi)/d\xi$ and $dh_r(\xi)/d\xi$, respectively, where ξ are the reference coordinates of the solution points. By setting $a = 1$ and applying upwinding at the interfaces,

$$J_j^{-1} \hat{f}_l^c = J_{j-1}^{-1} \hat{u}_{j-1}(1) \quad (12)$$

and

$$J_j^{-1} \hat{f}_r^c = J_j^{-1} \hat{u}_j(1) \quad (13)$$

By substituting Eqs. (12) and (13) into Eq. (11) and collecting the matrix operators into C_0 and C_{-1} ,

$$\frac{\partial \bar{u}_j}{\partial t} = -J_j^{-1} C_0 \mathbf{u}_j - J_{j-1}^{-1} C_{-1} \mathbf{u}_{j-1} \quad (14)$$

$$C_0 = \mathbf{D} - \mathbf{h}_l \mathbf{l}_l^T \quad (15)$$

$$C_{-1} = \mathbf{h}_l \mathbf{l}_r^T \quad (16)$$

where \mathbf{l}_l and \mathbf{l}_r are again compatible with Ref. [7] and defined such that \mathbf{l}_l^i is the contribution of the i th Lagrange basis function evaluated at the left interface. \mathbf{l}_r is similarly defined.

Defining the continuous input as a Bloch wave and projecting onto the discrete solution domain,

$$u(x, t) = v \exp(ikx - \omega t) \quad (17)$$

and

$$\mathbf{u}_j = \mathbf{v}_j \exp(ik(0.5(\xi + 1)\delta_j + x_j - ct)) \quad (18)$$

Inputting this result into Eq. (14) and setting $\delta_j = x_j - x_{j-1}$ give the following:

$$c(k) \mathbf{v} = -\frac{i}{k} \left(J_j^{-1} C_0 + J_{j-1}^{-1} C_{-1} \exp(-ik\delta_j) \right) \mathbf{v} \quad (19)$$

Equation (19) shows that the modified phase velocity $c(k)$ is one of the complex eigenvalues of a matrix describing the spatial transformation performed by the scheme. For an FR scheme with order p , there will be p eigenvalues to this problem, of which one is the physical result and the other modes are phase shifted values to give an orthogonal set. The physical interpretation of $c(k)$ is that a wave number's dispersion factor is $\Re(c(k))$ and its dissipation factor is $\Im(c(k))$.

The special case that $\delta_j = \text{const}$ implies that $J^{-1} = \text{const}$, which was the case investigated in [7,14]. However, the more general form of Eq. (19) allows the von Neumann analysis to be performed on stretched meshes. More important, Eq. (19) shows that the stencil of cells affecting the dissipation and dispersion of an upwinded FR scheme is just the current cell and its immediate neighbor, and hence only the local expansion rate is important for behavior. This is clearly not the case for finite difference schemes above the second order. Repeating the analysis for an FD scheme will give a basis of comparison and an example of the modified wave number for a fourth-order central difference scheme, which is given in Eq. (20):

$$c(k) = \frac{i}{k} \left(b_{-2,j} \exp(-ik(\delta_j + \delta_{j-1})) + b_{-1,j} \exp(-ik(\delta_j)) + b_{2,j} \exp(ik(\delta_{j+2} + \delta_{j+1})) + b_{1,j} \exp(ik(\delta_{j+1})) \right) \quad (20)$$

where $b_{-2,j}$ is a weighting factor from the derivative of the Lagrange polynomial basis function corresponding to point $j-2$ evaluated at point x_j , and so on.

A further implication of Eq. (18) is that Eq. (11) can be rewritten in a form called the update equation:

$$\frac{\partial \bar{u}_j}{\partial t} = Q \bar{u}_j \quad (21)$$

And, for the case of pure upwinding at the interface, it follows that $Q = -J_j^{-1} C_0 - J_{j-1}^{-1} C_{-1} \exp(-ik\delta_j)$. Putting the result into this form allows the analytical framework of Asthana and Jameson [14] to be used; hence,

$$\bar{u}_j(t + \tau) = R(Q) \bar{u}_j(t) \quad (22)$$

$$R_{33} = I + \frac{(\tau Q)^1}{1!} + \frac{(\tau Q)^2}{2!} + \frac{(\tau Q)^3}{3!} \quad (23)$$

Equation (23) is an example definition of R for a third-order three-step low-storage Runge–Kutta [28]. The form of Eq. (22) implies the von Neumann condition of the R spectral radius: $\rho(R) \leq 1 \forall k \in \mathbb{R}$.

From the analytical form, the main derived quantity to be considered is the points per wave wavelength (PPW) for a dispersion of less than 1%, which is defined as follows:

$$\text{PPW} = \frac{2\pi}{\{\hat{k} | \inf(|\Re(c(\hat{k})) - 1|_2, \epsilon)\}} \quad (24)$$

where ϵ is the error level, and $c(k)$ is the convective velocity from Eq. (19). This definition of the PPW is based on the points being the solution points in the case of FR. Consider the case of a wave for which the wavelength is the length of an element. The normalized Nyquist wave number would then be $2\pi/(p+1)$, and hence the use of solution points is captured by this definition. The PPW are particularly interesting because they can be used to produce minimum point requirements for a given region if the scale of flow features or the explicit filter width is known. A further derived quantity that will be touched on briefly is the implicit filter kernel (Trefethen [29]):

$$\hat{G}(\hat{k}) \propto e^{i\Re(c(\hat{k}))} \quad (25)$$

Although this is not the main subject of this paper, it can be illuminating to briefly look at the implicit filter.

To validate the analytical methods presented and gain insight into the fully discretized scheme behavior, a numerical approach is proposed that is similar to Lele's [26] analytical method. The methodology is to apply a scalar wave to a one-dimensional domain and allow the wave to be convected downstream. By choosing a low CFL number of 0.01, the spatial terms dominate the overall error. (CFL numbers of 0.05 and 0.005 were also tested, and the results

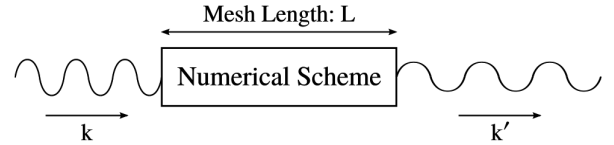


Fig. 3 Schematic of numerical scheme with incoming and outgoing wave showing wave number transformation over mesh of length L .

were found to be largely unchanged. They were only affected by the discrete Fourier transform because the sampling rate would vary with the CFL number. Hence, a CFL number of 0.01 was used to mitigate this error and give a fast test turnover time.) A Fourier analysis is then performed on the prescribed wave after convection through the grid. The transform of the field u is as follows:

$$\tilde{u}(x) = \sum_{k=-N/2}^{N/2} A_k \exp\left(\frac{2\pi i k x}{L}\right) \quad (26)$$

The method by Lele [26] would have, however, taken the spatial derivative of the wave after convection to give the following:

$$\tilde{u}'(x) = \sum_{k=-N/2}^{N/2} A_k \left(\frac{2\pi i k}{L}\right) \exp\left(\frac{2\pi i k x}{L}\right) \quad (27)$$

By dividing Eq. (27) by Eq. (26), the modified wave number can be obtained as in Eq. (28). In practice, this approach has low throughput, due to the need to calculate the derivative and as the full wave number space has to be explored. Furthermore, this method was found to be prone to the introduction of additional sources of error caused by the method used to calculate the derivative. Therefore, a direct comparison is made between the Fourier transform (FT) of the prescribed input wave and the FT of the prescribed wave after convection through the grid. This is schematically represented in Fig. 3:

$$k' = \left(\frac{L}{2\pi i}\right) \frac{\tilde{u}'(x)}{\tilde{u}(x)} \quad (28)$$

where k' is the modified wave number and equals $\omega/c(k)$. This method is used for calculation of the PPW for numerical test cases in accordance with Eq. (24).

IV. Analytical Testing

A. Spatial Characteristics

The analytical method presented in Sec. III makes the implicit assumption that there is a linear mapping between solution point placement in the real and physical domains. The analysis does, however, carry through the ability for the relative scaling of adjacent cells to be varied. Hence, this allows for the characteristics of nonuniform grids to be investigated, with the geometric expansion being one such linear transformation in common usage, for example, in the meshing of boundary layer. The geometric expansion is defined as follows:

$$x_{j+1} = x_j + \gamma(x_j - x_{j-1}) \quad (29)$$

where γ is the grid expansion rate. The points that this transformation defines are then used as the flux points for the element, and linear interpolation gives the solution points physical domain coordinates, using the computational quadrature as weight to ensure a linear mapping. Proceeding to analytically calculate the modified wave speed from Eq. (19), a preliminary result that can be qualitatively informative is the filter kernel, and it is shown in Fig. 4. In each case, the convolution kernel is normalized independently by the Nyquist wave number k_{ny} . This is included because it clearly shows that, although there is merit in going to much higher orders ($p > 4$), this does result in a case of diminishing returns.

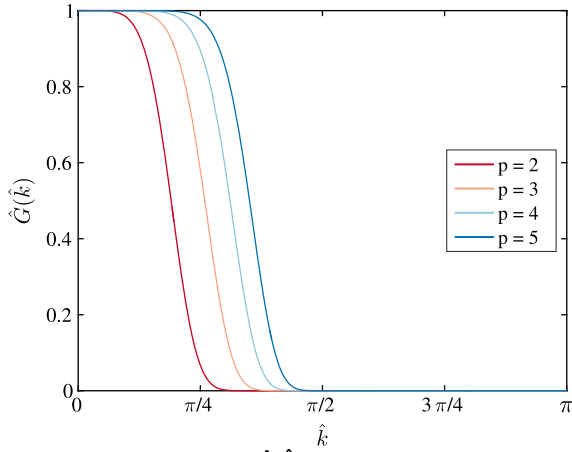


Fig. 4 Analytical filter kernel $\hat{G}(\hat{k})$ against Nyquist normalized wave number \hat{k} for various orders of upwinded FR with Huynh g_2 correction functions [6]. This is for $t = 100$.

Figures 5 and 6 shows normalized wave numbers against normalized modified wave numbers for differing levels of mesh stretching. The results for the uniform grid case can be compared to those found by Huynh [6] and found to be in agreement. What the new results broadly exhibit is dispersion overshoot for expanding grids, whereas contracting grids cause dispersion undershoot. For expanding meshes, this physically means that, for a central band of wave numbers, in which the group velocity ($\partial\omega/\partial k$) is not approximately constant, the upwind group velocity is higher. This is caused by the change in the Nyquist wave number between the smaller upwind and larger downwind elements in an expanding mesh. Resultantly, as the solution advects downwind, this small increase in the group velocity between elements means that a wave will be advected into an element faster than it will exit. This gives rise to antidissipation, seen in Fig. 6. The opposite behavior is exhibited in contractions. At wave numbers above this central band, Lagrange fitting becomes ineffective at sufficiently projecting the prescribed

wave into the functional space, and so the dispersion relation goes to zero regardless, and the dissipation becomes high.

To highlight the practical impact of mesh deformation, the PPW resulting in a dispersion error of less than 1% [Eq. (24) with $\epsilon = 0.01$] is plotted against the expansion factor in Fig. 7. Over the range of expansion factors, there are some clear optimal PPW at varying polynomial orders. When Fig. 5 is considered, it can be seen that the dispersion over- or undershoot present under some conditions can be counteracted by mesh warping. Therefore, depending on mesh conditions, it may be beneficial to directionally vary the spatial order because this may reduce the point requirements locally. For example, for an eddy passing through a complex mesh, fewer points will be needed while passing through a contraction with $p = 5$ as compared to $p = 4$, and vice versa. It is proposed that this could be achieved by maintaining the order of the polynomial interpolation, which is reflected in the number of solution points, but the order of the correction function could be varied. Clearly, this can only be used as a means of dropping the order accuracy, and not as a means of increasing order. From Vincent et al. [30], it can be seen that this method results in a special case of the energy stability criterion and that the correction functions proposed by Vincent et al. [30] with reduced order will still fulfill this criterion. A study was carried out to this effect, and it was found that using a p th order, as opposed to a $p + 1$ th order, correction function on a p th-order subdomain results in a stable degradation of the spatial order, pointing to the feasibility of this method.

B. Coupled Spatial–Temporal Characteristics

The preceding analysis was predicated on using an analytical solution to the linear advection equation that allowed the time derivative for the semidiscrete linear system to be exactly calculated. This was, of course, a simplification that could not be used practically; and Eq. (22) is far more representative of a real implementation. The family of temporal integration schemes to be coupled to FR here are low-storage Runge–Kutta (RK) [28], commonly called RK33, RK44, etc. The analysis performed is primarily in search of the maximum stable CFL number (τ/δ_j for $a = 1$) obtained via varying the time step τ and calculation of the

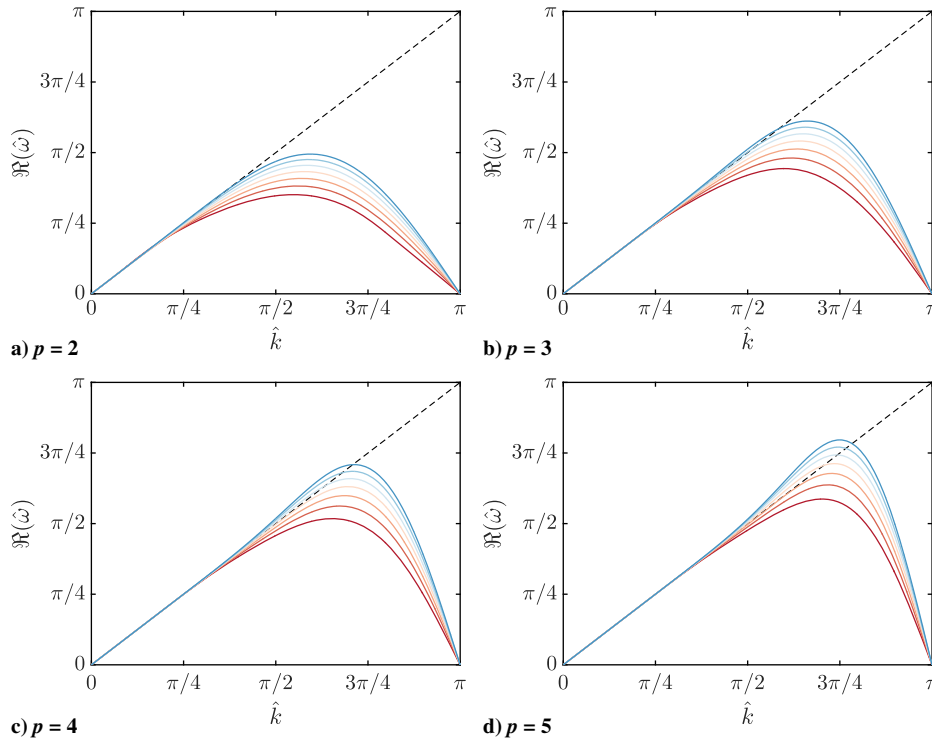


Fig. 5 Dispersion relations for FR, with Huynh g_2 correction functions [6], on various geometrically stretched meshes: -- spectral performance, $\gamma = 0.4$, $\gamma = 0.6$, $\gamma = 0.8$, $\gamma = 1.0$, $\gamma = 1.2$, $\gamma = 1.4$, and $\gamma = 1.6$.

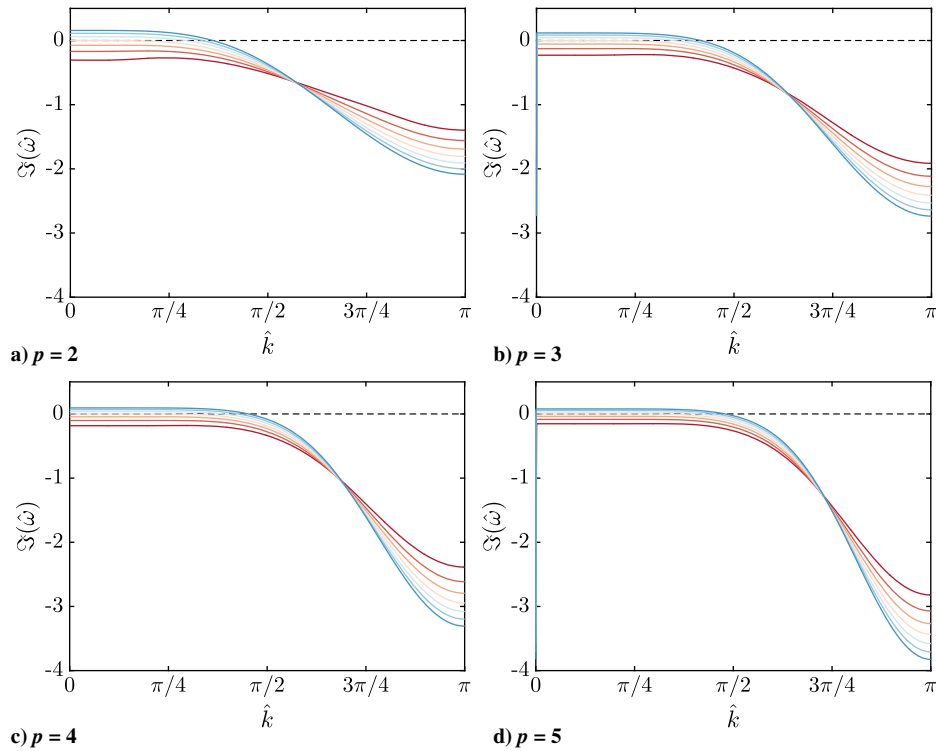


Fig. 6 Dissipation relations for FR, with Huynh g_2 correction functions [6], on various geometrically stretched meshes. --- spectral performance, — $\gamma = 0.4$, — $\gamma = 0.6$, — $\gamma = 0.8$, — $\gamma = 1.0$, — $\gamma = 1.2$, — $\gamma = 1.4$, — $\gamma = 1.6$.

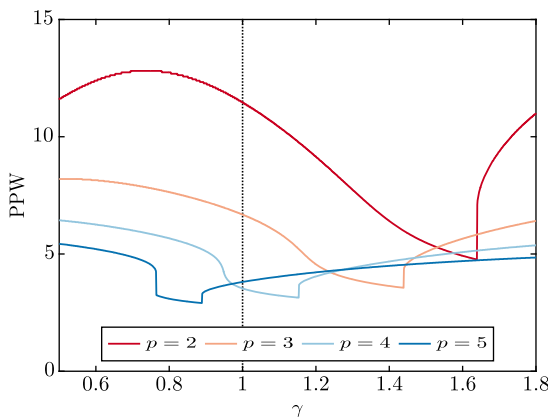


Fig. 7 PPW for error < 1% against expansion rate γ for various spatial orders of upwinded FR with Huynh g_2 correction functions [6].

spectral radius of the update matrix R . This is plotted in Fig. 8 for various geometric expansion ratios and is summarised for various orders in Fig. 9. Initially focusing on contracting grids, the maximum stable CFL number is shown to be higher than in the case of uniform grids. This could have been expected from observation of Fig. 6; furthermore, it can be reasoned that, as a wave is swept from one cell to its smaller upwind neighbor, the ability of the neighboring element to resolve that wave improves. This is due to the wave's Nyquist normalized wave number \hat{k} decreasing as it is advected through successively smaller elements.

Focusing on expanding grids, if the third order is considered, $p = 2$, $\rho(R) \not\leq 1 \forall \{k \in \mathbb{R} : \gamma > 1\}$; this means that, while being strictly unstable, some wave numbers are in practice stable. This is displayed in Fig. 9b, with $\rho(R(k))$ being both less than and greater than one. Note that τ is shown increasing as a decrease in color intensity. The practical implication is that a wave k fed into the expanding grid can cause an instability if $\rho(R(k)) > 1$, however, as the wave advects, the relative wave number increases due to a

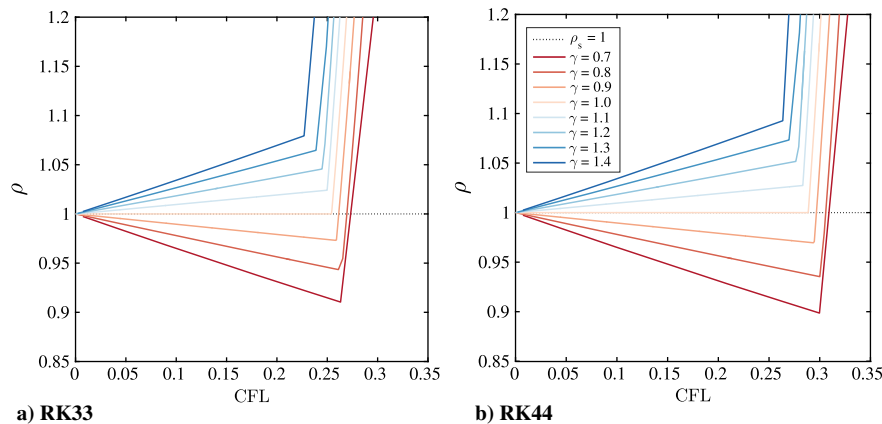


Fig. 8 Spectral radius of time scheme specific update matrix R for $p = 3$ upwinded FR with Huynh g_2 corrections [6] against CFL number on various grids.

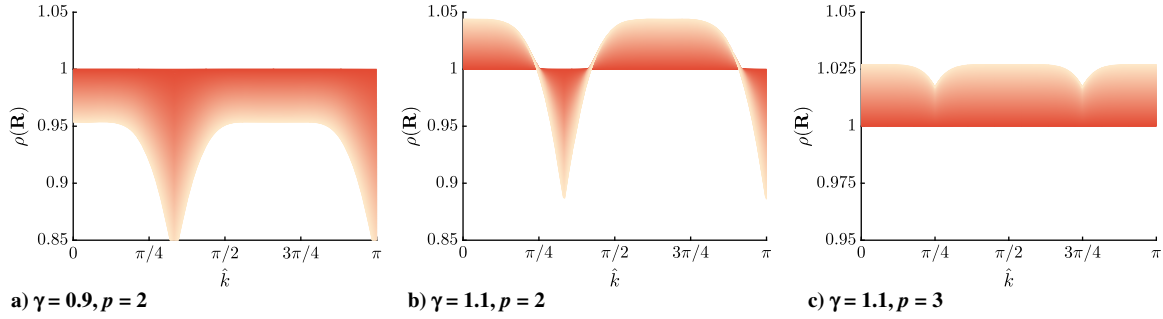


Fig. 9 Spectral radius of R for RK44 upwind FR with Huynh g_2 correction functions [6] against Nyquist normalized wave number for $\gamma = 0.9$ and $\gamma = 1.1$ with various time steps.

Table 1 Analytical CFL limit of FR for various grid expansion factors and temporal integration schemes, using the Huynh correction function [6]

Time scheme	Spatial order	CFL						
		$\gamma = 0.7$	0.8	0.9	1.0	1.1	1.2	1.3
RK33	3	0.519	0.482	0.463	0.448	0.442	0.436	0.424
	4	0.284	0.269	0.261	0.254	0.250	0.245	0.239
	5	0.183	0.177	0.172	0.167	0.164	0.161	0.159
RK44	3	0.592	0.547	0.531	0.513	0.505	0.495	0.507
	4	0.318	0.307	0.297	0.288	0.282	0.278	0.270
	5	0.218	0.199	0.194	0.189	0.186	0.182	0.179
RK55	3	0.702	0.634	0.611	0.590	0.579	0.567	0.558
	4	0.353	0.352	0.342	0.332	0.326	0.320	0.311
	5	0.246	0.230	0.224	0.217	0.214	0.210	0.204

decreasing k_{nq} . Hence, a band of $\rho(R(k)) < 1$ will be encountered by the wave and the instability will be attenuated. This procedure would be expected to repeat until the wave was beyond the grid resolution.[§]

For $p > 2$, different expanding mesh characteristics are seen with $\rho(R) \geq 1 \forall \{k \in \mathbb{R}: \gamma > 1\}$ (Fig. 9c). Later numerical tests will show that, for $p > 2$, the instability is also encountered, but this is likewise attenuated as the wave advects. This result can be seen analytically by observing the dissipation relation in Fig. 6 and using the same logic as before. The full impact on stability that this implies will be discussed later alongside numerical findings. However, for simplicity, the scheme stability limit (as shown in Table 1) will be taken as the higher point between either the point of the sharp increase in the spectral radius or the point at which the spectral radius increases above one (see Fig. 8).

V. Numerical Results

A. Grid Stretching for Linear Advection

The analytical procedures set out up to this point have been semidiscrete and idealized. For CFD practitioners, the comparative performance and the implemented performance of FR is highly important. From this, the process of mesh generation can be informed as well as greater understanding of the expected results gained. To this end, numerical tests are performed for wave numbers $0 \leq k \leq k_{nq}$, where k_{nq} is the Nyquist wave number for a uniform mesh of unit length. For the purposes of comparison, k and k' (the modified wave number) are normalized by the mesh-averaged Nyquist wave number. This gives $0 \leq \hat{k} = \pi k/k_{nq} \leq \pi$ and $0 \leq \hat{k}' = \pi k'/k_{nq} \leq \pi$.

Finite difference schemes are used to provide a comparison akin to high-quality industrial codes. At higher orders, central difference schemes begin to become unstable because, for unstretched grids, second-order and greater central difference schemes offer no

dissipation. Therefore, the only sources of numerical error are from dispersion and temporal integration. Because of this, and as increasing order leads to better dispersion performance, the cell Reynolds number increases. The result is that FD schemes at intermediate wave numbers become unable to damp out disturbances. (It must be noted that, due to the very low CFL number, the temporal scheme introduces negligible numerical error.) This is combated by adding smoothing to the solution, which is a common practice in industry; and it is here accomplished by adding a small amount (0.5–2%) of Lax–Friedrichs differencing.

Two key points are highlighted by Fig. 10a. [The analytical results shown are found from Eq. (19) and a similar analysis.] The first of these is that FR requires fewer PPW than FD schemes at an equivalent order. More important, this means that coarser meshes can be used by FR for similar wave resolving characteristics to FD schemes at the same order. It is believed that the increased accuracy of FR originates from the polynomial reconstruction in a reference subdomain; hence, the propagation of information in FR is largely controlled by the correction function, which can lead to superior performance. FD methods use a stencil, for which information can freely propagate through; hence, a less coherent solution is produced due to each point effectively producing its own polynomial fit of the solution.

Second, Fig. 10a shows a discrepancy between the theoretical and analytical results for both FR and FD. The origin of the error in both of these schemes is the numerical diffusion. For FD, this is due to the scheme's subtle instability, meaning that, for useful implementation, some diffusion must be added to ensure the survival of the solution. FR is also affected by numerical diffusion, but this is caused by its own intrinsic dissipation, which is apparent in Fig. 6. When numerical tests are run, the dispersion and dissipation are inseparable and, although a dispersion relationship of sorts can be found, it is impacted by the dissipation of the scheme damping out higher wave numbers. This is the reality of any application of a scheme, and so it can be informative to run both analytical and numerical tests because the numerically derived PPW shown in Fig. 10a are those that an end user will experience. The same effect can be seen in Fig. 10b: as the mesh becomes stretched, the PPW rise more quickly than the analytical results would predict. This is caused by the onset of dissipation at lower wave numbers for deformed meshes but, importantly, a wave passed through a multielement mesh will have the transfer function applied multiple times, thereby causing greater attenuation.

The results of great significance displayed both numerically and analytically show that FR has the ability to resolve waves better than FD schemes and that FR is more numerically robust when applied to geometrically stretched meshes, with FR requiring 33% of the mesh points compared to FD in 1-D for severely stretched meshes ($\gamma = 1.2$ at fourth order). Moving to two or three dimensions, this result, in the most extreme examples, can be 11 or 4%, respectively. The increased ability of FR to handle stretched meshes is again because of the localized fitting within subdomains; here, the linear transformation caused by the stretching of the elements is exactly captured in the Jacobian. For this case, the impact of adjacent cell stretching is felt only through convection of the solution through one interface. However, for a fully compressible Euler or Navier–Stokes implementation, the effect of adjacent cells could be increased

[§]Also of note from Fig. 9 is that the spectral radius is a periodic function that depends on the element Nyquist wave number rather than the solution point Nyquist wave number.

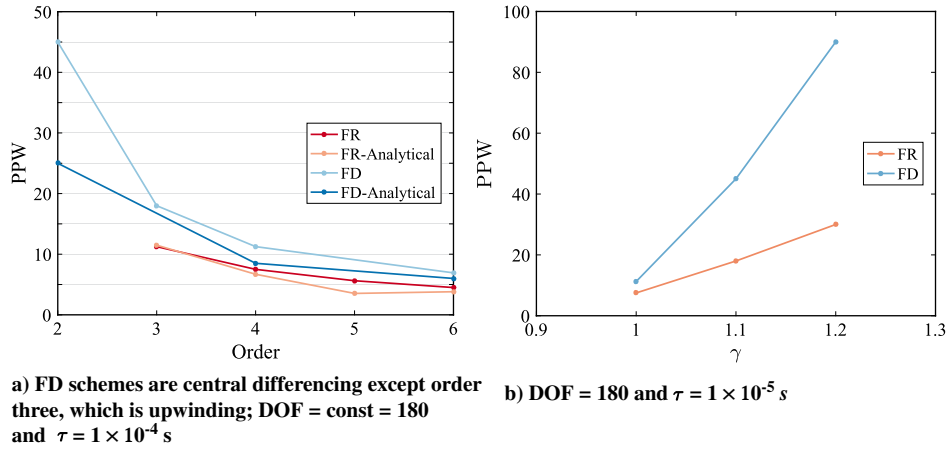


Fig. 10 PPW a) for 1% error against spatial order of FD and FR schemes and b) against mesh stretching factor for fourth-order FD and FR schemes.

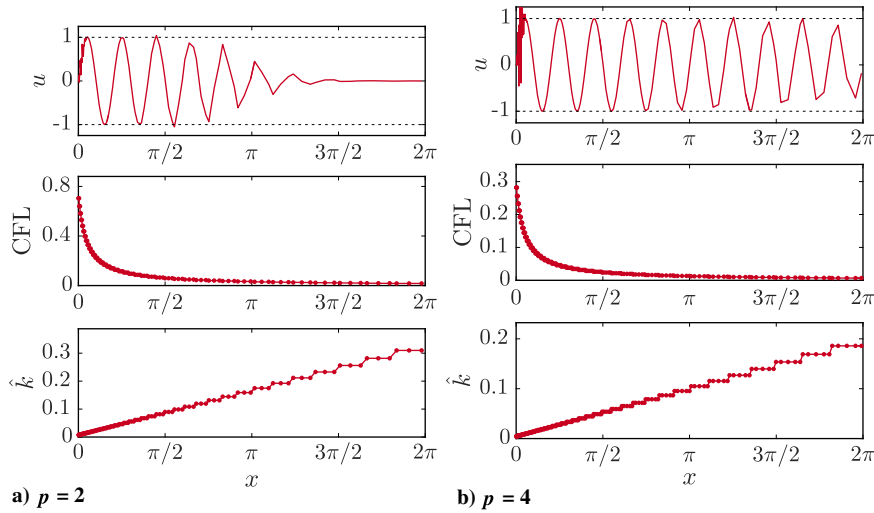


Fig. 11 For third- and fifth-order FRs on an expanding grid with $\gamma = 1.1$ using RK44 time integration, a spatial slice is shown with the convected parameter u , the CFL number, and the Nyquist normalized ($k = \pi k/k_{nq}$).

because Riemann solvers at all interfaces would be necessary and would give rise to more intercell communication.

To further understand the stability of the full numerical scheme, it is necessary to consider the spatiotemporal coupling. In the previous section, the effect of this coupling was considered and it was said that, for $p \geq 3$ on expanding grids, the behavior was slightly different, i.e., $\rho(R) \geq 1 \forall k$. The implication this has for the stability of higher-order expanding grids is not clear from the spectral radius; however, as the wave moves through the expanding grid, k will increase, and so the scheme dissipation will add a stabilizing effect. To show this, a similar numerical method is used; however, it now takes a spatial slice for various orders, wave numbers, and grids. Figure 11 shows two such slices. Initially, the fed wave shows some instability, but advection through the grid means dissipation from the spatial scheme will begin to cancel some of the negative dissipation of the time scheme. The result is that, after an initial band of instability, both orders show recovery of the solution before beginning to decay on the sparser cells.

This also illustrated a limitation of the analytical approach adopted here: that taking a solution of the form of Eq. (17) means that the solution is static, i.e., evolutions of the solution from far upstream are not permitted. Again, this emphasizes the importance of running numerical tests alongside analytical ones.

B. Grid Warping for the Euler Equations

Few problems confronted in engineering are ever sufficiently simple that they can be solved with sufficient accuracy by 1-D methods, making extension to higher dimensionality crucial. Two dimensions also allow for a greater range of geometrical deformations to occur,

even while maintaining a linear transformation of elements. Included within this, each element has a higher number of degrees of freedom, revealing a potential mechanism for inaccuracies to enter the solutions. To evaluate the effect of higher dimensionality, the isentropic convecting vortex (ICV) test case is used because it has a known analytical solution, and so the numerical error can be straightforwardly calculated for the Euler equations. A mixture of mesh qualities is to be tested, and so the mesh quality is artificially reduced by stochastically jittering corner nodes of a uniform grid via time-seeded random numbers. The degree of jitter is controlled by a multiplying factor, and the mesh quality and warp are then characterized by a skew angle. This is defined as the mesh average absolute angle by which the element cross diagonals deviate from square (Fig. 12) and encompass both the

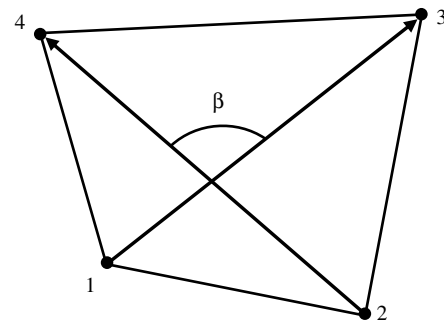


Fig. 12 Cross-diagonal angle definition: $\alpha = \beta - 90^\circ$.

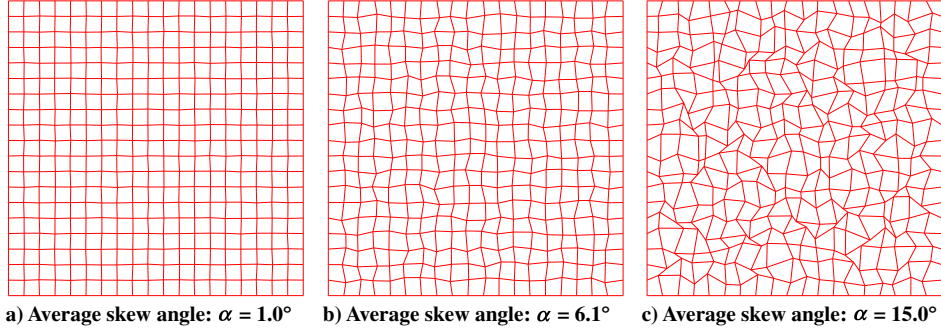


Fig. 13 19×19 quadrilateral meshes showing differing degrees of node jittered mesh warp.

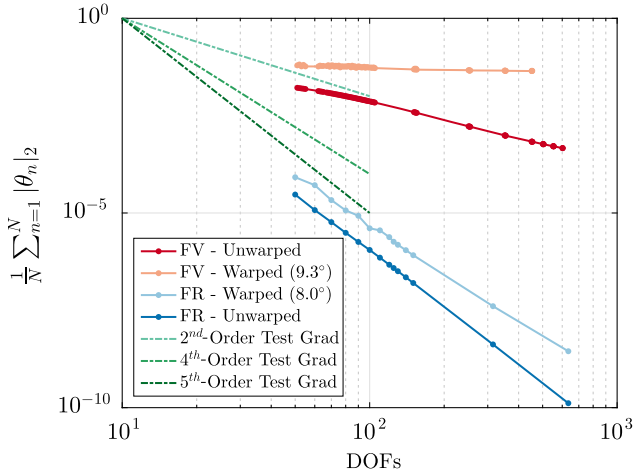
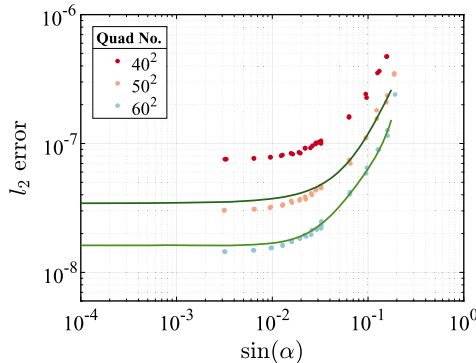


Fig. 14 Point-averaged l_2 norm of error $1/N \sum_{n=1}^N |\theta_n|_2$ against DOFs for $p = 4$ FR and a nominally second-order FV scheme. CFL = 0.01 for 3000 time steps (Grad, Gradient).

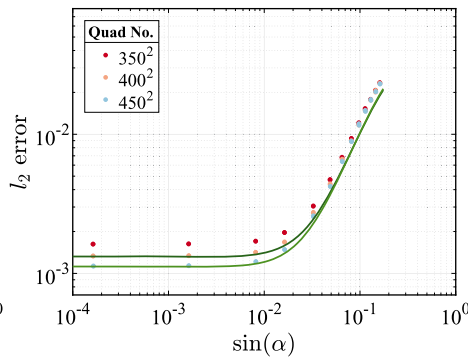
skewness and the aspect ratio of a mesh. Some sample meshes are shown in Figs. 13a–13c.

A finite volume scheme (a simplified version of T block) with the same explicit time integration as used in the FR calculation is used for performance comparison, as it is representative of a family of schemes widely used in industry. To evaluate the spatial error, the temporal error has to be minimized by use of an appropriately small time step, which in this case corresponds to CFL = 0.01. (CFL = 0.05 and 0.005 were also tested, and the error was found to be independent of the temporal scheme at this level.) By comparing the exact solution u and computed solution u' the error θ can be calculated and the spatial order of accuracy (OOA) can be obtained:

$$\theta = u - u' = \mathcal{O}(\delta^{p+1}) \quad (30)$$



a) Magnitude of mesh warp against error for various mesh densities using an FR scheme $p = 4$ (•)



b) Magnitude of warp against error for various mesh densities using an FV scheme (•)

Fig. 15 Magnitudes of a) mesh warp against error for various mesh densities using an FR scheme of $p = 4$ (•) and b) warp against error for various mesh densities using an FV scheme (•).

Recovery of the spatial OOA is shown in Fig. 14 (i.e., OOA = $p + 1$), and a comparison can be made with the fifth-order test gradient to see this. The plotted results for the FV scheme display OOA ≈ 2 , as well as a large increase in the cell-averaged l_2 error as compared to FR for the same number of degrees of freedom (DOFs). Also shown in Fig. 14 are the results of moderate mesh warping. In FR's case, a move toward OOA ≈ 4 occurs, and the FV scheme result becomes aphysical, i.e., OOA = 0.

A more detailed investigation into the deterioration of the spatial order was performed via variation of the degree of node jittering. Tests were run with CFL = 0.01 for 500 time steps (again, results were found to be independent of the CFL number at this level). The results of the numerical tests and a predictive procedure are shown in Fig. 15. The predictive procedure used the error data from a mesh of fewer degrees of freedom together with the desired OOA to make a prediction of the error at a higher quantity of degrees of freedom.

Figure 15 shows that, consistent with Fig. 14, at low skew angles, FR's OOA is unaffected by mesh quality: OOA $\rightarrow p + 1$ as $\alpha \rightarrow 0$ deg. Figure 15a then confirms that, on poorer-quality meshes, the OOA drops by approximately one, which is here shown as a drop from OOA = 5 to OOA ≈ 4 ; this is shown by comparison to the fourth-order predicted error line. This warp-induced change occurs at $\alpha \approx 1.5$ deg and, as mesh skewness increases to its maximum, FR is still able to give an accurate solution. (Also plotted are the predicted error values for fourth-order recovery, shown by solid lines.) By comparison, the FV scheme (Fig. 15b) undergoes a warp-induced error change at $\alpha \approx 0.55$ deg, transitioning from OOA ≈ 2 to OOA = 0. Although the FV scheme is much simpler, this shows that the performance of such schemes widely used in industry can be rapidly eroded by a lack of mesh quality. [Also plotted is the predicted error based on the order recovered from Fig. 14 (shown with solid lines). The DOFs are chosen to be comparable to the DOFs for the FR tests.]

The root cause of the loss of order accuracy of FR on warped grids is not fully revealed by these tests. The Jacobian that maps between the physical and computational domain in this case provides an exact

Table 2 Comparable errors in a 2-D ICV test for FR and FV schemes

	Flux reconstruction	Finite volume
Point-averaged error	4.7×10^{-5}	4.01×10^{-5}
Wall time, s	1.6	639
Cells	64, $p = 4$	4,000,000

mapping due to the node jittering providing a linear transformation. Hence, error is not introduced to the convective velocity through the Jacobian. The additional error has two potential sources. First, the linear component of FR could introduce error via ill conditioning of the projection to the functional space when waves are advected at an angle. Second, Jameson et al. [31] derived the aliasing error for 1-D nonlinear problems in the FR framework; yet, in higher dimensions, and on arbitrary grids, cross multiplication of projection terms will be present. Therefore, as the mesh becomes skewed, aliasing has the scope to introduce larger quantities of error. Both of these topics are quite expansive and are left for further investigation.

As a final aside to illustrate the increase in performance that FR offers as compared to a typical FV method, the ICV test case on a uniform mesh was used. For this test, the number of degrees of freedom was varied such that the grid-averaged l_2 error was comparable; this was done with CFL = 0.01 for 100 time steps. (A small variation of the CFL number was made, and the results were found to be invariant with the CFL number.) The test was carried out on a single core of an Intel® Xeon® L5630, which was otherwise idle. The results of testing are shown in Table 2, and they show that FR requires ~2.6 orders of magnitude less wall time for the same error in 2-D as the FV method used here.

VI. Conclusions

The use of flux reconstruction (FR) on warped meshes is important for the likely future applications of the scheme. It is that FR is more resilient to distorted meshes than some finite difference and finite volume (FV) families of schemes that are currently widely used in industry. A detailed look at the points per wave wavelength of FR on stretched grids with varying order, as well as study of the FR stability criterion, shows that, depending on geometry, the order of the scheme can be varied to increased performance. In particular, within a given cell, the correction function order can be directionally varied to increase wave-resolving ability. It is also shown from the linear advection equation that the Courant–Friedrichs–Lewy limit with nonregular grids is dependent on the dominant wave direction, with contracting grids providing a stabilizing effect. This is a feature of FR that will impact boundary-layer meshes. It is proposed that the ill-conditioning of the functional projection of FR causes the degradation in accuracy for warped meshes. A more complete study of this is left as future work. Lastly, in some runtime comparisons, FR is found to require ~2.6 orders of magnitude less wall time for the same error in two-dimensional tests as compared to a widely used FV method.

Acknowledgment

The support of the Engineering and Physical Sciences Research Council of the United Kingdom is gratefully acknowledged.

References

- [1] Piomelli, U., "Wall-Layer Models for Large-Eddy Simulations," *Progress in Aerospace Sciences*, Vol. 44, No. 6, 2008, pp. 437–446. doi:10.1016/j.paerosci.2008.06.001
- [2] Tucker, P., Eastwood, S., Klostermeier, C., Jefferson-Loveday, R., Tyacke, J., and Liu, Y., "Hybrid LES Approach for Practical Turbomachinery Flows: Part 1—Hierarchy and Example Simulations," *ASME Turbo Expo 2010: Power for Land, Sea and Air*, Vol. 134, American Soc. of Mechanical Engineers, Fairfield, NJ, 2010, pp. 1–13.
- [3] Tucker, P., "Unsteady Computational Fluid Dynamics in Aeronautics," *Fluid Mechanics and Its Applications*, 1st ed., Vol. 104, Springer, Dordrecht, The Netherlands, 2014, pp. 1–66.
- [4] Chow, F. K., and Moin, P., "A Further Study of Numerical Errors in Large-Eddy Simulations," *Journal of Computational Physics*, Vol. 184, No. 2, 2003, pp. 366–380. doi:10.1016/S0021-9991(02)00020-7
- [5] Ghosal, S., "An Analysis of Numerical Errors in Large-Eddy Simulations of Turbulence," *Journal of Computational Physics*, Vol. 125, No. 1, 1996, pp. 187–206. doi:10.1006/jcph.1996.0088
- [6] Huynh, H. T., "A Flux Reconstruction Approach to High-Order Schemes Including Discontinuous Galerkin Methods," *18th AIAA Computational Fluid Dynamics Conference*, AIAA Paper 2007-4079, 2007, pp. 1–42.
- [7] Vincent, P. E., Castonguay, P., and Jameson, A., "Insights from von Neumann Analysis of High-Order Flux Reconstruction Schemes," *Journal of Computational Physics*, Vol. 230, No. 22, 2011, pp. 8134–8154. doi:10.1016/j.jcp.2011.07.013
- [8] Huynh, H. T., "A Flux Reconstruction Approach to High-Order Schemes Including Discontinuous Galerkin for Diffusion," *47th AIAA Aerospace Science Meeting*, AIAA, Reston VA, June 2009, pp. 1–34.
- [9] Castonguay, P., Williams, D. M., Vincent, P. E., and Jameson, A., "Energy Stable Flux Reconstruction Schemes for Advection-Diffusion Problems," *Computer Methods in Applied Mechanics and Engineering*, Vol. 267, No. 1, 2013, pp. 400–417. doi:10.1016/j.cma.2013.08.012
- [10] Huynh, H. T., "High-Order Methods Including Discontinuous Galerkin by Reconstructions on Triangular Meshes," *49th AIAA Aerospace Sciences Meeting*, AIAA Paper 2011-0044, pp. 1–28.
- [11] Williams, D. M., and Jameson, A., "Energy Stable Flux Reconstruction Schemes for Advection-Diffusion Problems on Tetrahedra," *Journal of Scientific Computing*, Vol. 59, No. 3, 2014, pp. 721–759. doi:10.1007/s10915-013-9780-2
- [12] Sheshadri, A., "An Analysis of Stability of the Flux Reconstruction Formulation with Applications to Shock Capturing," Ph.D. Thesis, Stanford Univ., Stanford, CA, 2016.
- [13] Vincent, P. E., Farrington, A. M., Witherden, F. D., and Jameson, A., "An Extended Range of Stable-Symmetric-Conservative Flux Reconstruction Correction Functions," *Computer Methods in Applied Mechanics and Engineering*, Vol. 296, Nov. 2015, pp. 248–272. doi:10.1016/j.cma.2015.07.023
- [14] Asthana, K., and Jameson, A., "High-Order Flux Reconstruction Schemes with Minimal Dispersion and Dissipation," *Journal of Scientific Computing*, Vol. 62, No. 3, March 2015, pp. 913–944. doi:10.1007/s10915-014-9882-5
- [15] Asthana, K., López-Morales, M. R., and Jameson, A., "Non-Linear Stabilization of High-Order Flux Reconstruction Schemes via Fourier-Spectral Filtering," *Journal of Computational Physics*, Vol. 303, 2015, pp. 269–294. doi:10.1016/j.jcp.2015.09.041
- [16] Chung, Y. M., and Tucker, P. G., "Accuracy of Higher-Order Finite Difference Schemes on Nonuniform Grids," *AIAA journal*, Vol. 41, No. 8, 2003, pp. 1609–1611. doi:10.2514/2.2117
- [17] You, D., Mittal, R., Wang, M., and Moin, P., "Analysis of Stability and Accuracy of Finite-Difference Schemes on a Skewed Mesh," *Journal of Computational Physics*, Vol. 213, No. 1, 2006, pp. 184–204. doi:10.1016/j.jcp.2005.08.007
- [18] Mengaldo, G., De Grazia, D., Vincent, P. E., and Sherwin, S. J., "On the Connections Between Discontinuous Galerkin and Flux Reconstruction Schemes: Extension to Curvilinear Meshes," *Journal of Scientific Computing*, Vol. 67, No. 3, 2016, pp. 1272–1292. doi:10.1007/s10915-015-0119-z
- [19] Kopriva, D. A., "Metric Identities and the Discontinuous Spectral Element Method on Curvilinear Meshes," *Journal of Scientific Computing*, Vol. 26, No. 3, 2006, pp. 301–327. doi:10.1007/s10915-005-9070-8
- [20] Sheshadri, A., Crabill, J., and Jameson, A., "Mesh Deformation and Shock Capturing Techniques for High-Order Simulation of Unsteady Compressible Flows on Dynamic Meshes," *SciTech 2015*, AIAA Paper 2015-1741, Jan. 2015, pp. 1–15.
- [21] Castonguay, P., "High-Order Energy Stable Flux Reconstruction Schemes for Fluid Flow Simulations on Unstructured Grids," Ph.D. Thesis, Stanford Univ., Stanford, CA, 2012.
- [22] Reed, W. H., and Hill, T. R., "Triangular Mesh Methods for the Neutron Transport Equation," Los Alamos National Labs. Rept. LA-UR-73-479, Albuquerque, NM, 1973.
- [23] Roe, P. L., "Approximate Riemann Solvers, Parameter Vectors, and Difference Schemes," *Journal of Computational Physics*, Vol. 43, No. 2,

- 1981, pp. 357–372.
doi:10.1016/0021-9991(81)90128-5
- [24] van Leer, B., *Fourteenth International Conference on Numerical Methods in Fluid Dynamics*, Lecture Notes in Physics, Feb. 1982, pp. 11–15.
doi:10.1007/3-540-11948-5
- [25] Harten, A., Lax, P. D., and van Leer, B., “On Upstream Differencing and Godunov-Type Schemes for Hyperbolic Conservation Laws,” *SIAM Review*, Vol. 25, No. 1, 1983, pp. 35–61.
doi:10.1137/1025002
- [26] Lele, S. K., “Compact Finite Difference Schemes with Spectral-Like Resolution,” *Journal of Computational Physics*, Vol. 103, No. 1, 1992, pp. 16–42.
doi:10.1016/0021-9991(92)90324-R
- [27] Hesthaven, J. S., and Warburton, T., “Nodal Discontinuous Galerkin Methods: Algorithms, Analysis, and Applications,” *Texts in Applied Mathematics*, 1st ed., Vol. 54, Springer, New York, 2008, pp. 75–133, Chap. 4.
- [28] Kennedy, C. A., Carpenter, M. H., and Lewis, R. M., “Low-Storage, Explicit Runge–Kutta Schemes for the Compressible Navier–Stokes Equations,” *Applied Numerical Mathematics*, Vol. 35, No. 1, 2000, pp. 177–219.
doi:10.1016/S0168-9274(99)00141-5
- [29] Trefethen, L. N., *Finite Difference and Spectral Methods for Ordinary and Partial Differential Equations*, 1st ed., Ithaca, NY, 1994.
- [30] Vincent, P. E., Castonguay, P., and Jameson, A., “A New Class of High-Order Energy Stable Flux Reconstruction Schemes,” *Journal of Scientific Computing*, Vol. 47, No. 1, 2011, pp. 50–72.
doi:10.1007/s10915-010-9420-z
- [31] Jameson, A., Vincent, P. E., and Castonguay, P., “On The Non-Linear Stability of Flux Reconstruction Schemes,” *Journal of Scientific Computing*, Vol. 50, No. 2, 2012, pp. 434–445.
doi:10.1007/s10915-011-9490-6

H. Blackburn
Associate Editor